

Families of subcritical spirals in highly counter-rotating Taylor-Couette flow

Alvaro Meseguer,^{1,*} Fernando Mellibovsky,¹ Marc Avila,² and Francisco Marques¹
¹*Departament de Física Aplicada, Universitat Politècnica de Catalunya, 08034 Barcelona, Spain*
²*Max-Planck Institute for Dynamics and Self-Organization, 37073 Göttingen, Germany*

(Received 21 November 2008; revised manuscript received 4 February 2009; published 20 March 2009)

A comprehensive numerical exploration of secondary finite-amplitude solutions in small-gap Taylor-Couette flow for high counter-rotating Reynolds numbers is provided, using Newton-Krylov methods embedded within arclength continuation schemes. Two different families of rotating waves have been identified: short axial wavelength subcritical spirals ascribed to centrifugal mechanisms and large axial scale supercritical spirals and ribbons associated with shear dynamics in the outer linearly stable radial region. This study is a first step taken in order to provide the inner structure of the skeleton of equilibria that may be responsible for the intermittent regime usually termed as *spiral turbulence* that has been reported by many experimentalists in the past.

DOI: 10.1103/PhysRevE.79.036309

PACS number(s): 47.20.Ft, 47.35.-i

I. INTRODUCTION

Subcritical transition to turbulence in shear flows has been studied for over a century and still remains an unsolved fundamental problem of hydrodynamic stability theory. Canonical open shear flows such as *plane Couette* (flow between inertially sliding parallel plates) or *pipe Poiseuille* (flow in an infinite pipe of circular cross section driven by a pressure gradient) exhibit subcritical transition to turbulence without mediation of a local bifurcation of their basic Navier-Stokes solution. These flows are linearly stable for all Reynolds numbers [1,2] although they undergo transition to turbulence in practice. For *plane Poiseuille* (flow between parallel plates driven by a pressure gradient), even though there is a subcritical Hopf bifurcation [3] of the plane Poiseuille parabolic profile for Reynolds number $Re=5772$, in practice this flow becomes turbulent for Reynolds numbers as low as 1800. Therefore, finite-amplitude perturbations must be responsible for transition in this regime. The stability of open shear flows with respect to finite-amplitude perturbations has been studied experimentally in the 1970s [4] and numerically in the 1980s [5–7] and 1990s [8,9], although this matter has recently regained much attention due to the discovery of a large variety of finite-amplitude solutions of the Navier-Stokes problem for plane Couette and pipe flows [10–13] which rely on the self-sustaining mechanism of near-wall turbulence within a minimal flow unit [14–17].

Open shear flows share many common drawbacks when studying the long-term behavior of turbulent or intermittent regime. In plane Poiseuille or pipe experiments, intermittent turbulent spots or puffs are advected downstream and sooner or later leave the domain. Numerically, the imposed periodicity in the streamwise direction not only overlooks the real boundary flow conditions at the entrance and exit of the domain, but it also may artificially reinfect the leading and trailing edges of localized spots, potentially leading to biased *lifetime* measurements of those structures [18–20].

The aforementioned difficulties can be overcome by working within a naturally streamwise-periodic problem

such as Taylor-Couette flow (TCF) between independently rotating concentric cylinders. Starting with the celebrated work of Taylor [21], TCF has been one of the most explored problems of fluid dynamics in the last century, being an experimental, theoretical, and numerical benchmark problem for bifurcation and hydrodynamic stability theories. TCF may exhibit a huge variety of secondary supercritical steady, time periodic, or almost periodic laminar flows before an eventual transition to chaotic regimes [22]. We refer the reader to standard monographs and references therein [23,24]. However, the subcritical hysteretic nature of the narrow-gap counter-rotating TCF has received little attention. Subcritical phenomena of TCF were first reported in the past by Coles [25] and Van Atta [26] in the 1960s who observed intermittent spiral patterns (usually termed as spiral turbulence) below the linear stability boundary of the basic circular Couette flow (CCF). Linear nonmodal analysis has shown a strong correlation between the hysteretic effects of spiral turbulence and transient growth of infinitesimal perturbations of the basic flow [27]. Recent experiments have addressed the similarities between the coherent nature of spiral turbulence in plane Couette and Taylor-Couette flows [28]. On those lines, recent numerical explorations have identified parameter ranges in the narrow-gap limit of TCF where some of the characteristics of the plane Couette flow can be recovered [29].

In this work we provide a comprehensive numerical exploration of rotating wave solutions in the counter-rotating TCF for a small gap case frequently used by former experimentalists and in nearby situations where spiral turbulence may already be observed. This work addresses the subcritical nature of short-wavelength spiral patterns that bifurcate from the centrifugally unstable region of the CCF as well as other exact solutions characterized by much longer axial wavelengths ascribed to the linearly stable shear region, some of them not bifurcating from CCF.

This paper is structured as follows. In Sec. II we provide the mathematical formulation of the problem. Section II A is devoted to describe the solenoidal spectral method used to discretize the Navier-Stokes equations. In Sec. II B we particularize our formalism for the search of rotating waves, reducing the original problem to a system of nonlinear algebraic equations. Section III describes the linear stability

*alvar@fa.upc.es

analysis of the CCF. The critical axial and azimuthal wave numbers found in the stability analysis are used in Secs. III A and III B in order to find high and low axial wave-number rotating waves, respectively.

II. MATHEMATICAL FORMULATION

We consider an incompressible fluid of kinematic viscosity ν and density ϱ contained between two concentric rotating cylinders whose inner and outer radii and angular velocities are r_i^* , r_o^* , and Ω_i and Ω_o , respectively. The independent dimensionless parameters appearing in this problem are the radius ratio $\eta=r_i^*/r_o^*$, which fixes the geometry of the annulus, and the Couette flow Reynolds numbers $R_i=dr_i^*\Omega_i/\nu$ and $R_o=dr_o^*\Omega_o/\nu$ of the rotating cylinders, where $d=r_o^*-r_i^*$ is the gap between the cylinders. Henceforth, all variables will be rendered dimensionless using d , d^2/ν , and ν^2/d^2 as units for space, time, and the reduced pressure ($p=p^*/\varrho$), respectively. The Navier-Stokes equation and the incompressibility condition become

$$\partial_t \mathbf{v} + (\mathbf{v} \cdot \nabla) \mathbf{v} = -\nabla p + \Delta \mathbf{v}, \quad \nabla \cdot \mathbf{v} = 0, \quad (1)$$

where $\mathbf{v}=(u, v, w)$ are the velocity components in cylindrical coordinates (r, θ, z) , satisfying the boundary conditions $v(r_i)=R_i$ and $v(r_o)=R_o$, where $r_i=r_i^*/d$ and $r_o=r_o^*/d$ are nondimensional. The basic CCF is $\mathbf{v}_B=(u_B, v_B, w_B)=(0, Ar+B/r, 0)$ with $A=(R_o-\eta R_i)/(1+\eta)$ and $B=\eta(R_i-\eta R_o)/(1-\eta)(1-\eta^2)$. We will assume that the flow is L^* periodic in the axial direction, so that the dimensionless domain is

$$(r, \theta, z) \in \mathcal{D} = [r_i, r_o] \times [0, 2\pi] \times [0, \Lambda], \quad (2)$$

where $\Lambda=L^*/d$ is the *aspect ratio* of the computational box.

In order to study the stability of the basic solution, the flow is split up into the basic velocity field \mathbf{v}_B and pressure p_B , along with their respective perturbations \mathbf{u} and q as follows:

$$\mathbf{v}(r, \theta, z, t) = \mathbf{v}_B(r) + \mathbf{u}(r, \theta, z, t), \quad (3)$$

$$p(r, \theta, z, t) = p_B(r) + q(r, \theta, z, t), \quad (4)$$

with

$$\nabla \cdot \mathbf{u} = 0, \quad \mathbf{u}(r=r_i) = \mathbf{u}(r=r_o) = \mathbf{0}, \quad (5)$$

i.e., \mathbf{u} is a solenoidal velocity field vanishing at the cylinder walls. On introducing the perturbed fields in the Navier-Stokes equations (1), we obtain a nonlinear initial-boundary problem for the perturbations \mathbf{u} and q ,

$$\partial_t \mathbf{u} = -\nabla q + \Delta \mathbf{u} - (\mathbf{u} + \mathbf{v}_B) \cdot \nabla (\mathbf{u} + \mathbf{v}_B), \quad (6)$$

$$\nabla \cdot \mathbf{u} = 0, \quad (7)$$

$$\mathbf{u}(r_i, \theta, z, t) = \mathbf{u}(r_o, \theta, z, t) = \mathbf{0}, \quad (8)$$

$$\mathbf{u}(r, \theta + 2\pi, z, t) = \mathbf{u}(r, \theta, z, t), \quad (9)$$

$$\mathbf{u}(r, \theta, z + \Lambda, t) = \mathbf{u}(r, \theta, z, t), \quad (10)$$

$$\mathbf{u}(r, \theta, z, 0) = \mathbf{u}_0, \quad \nabla \cdot \mathbf{u}_0 = 0 \quad (11)$$

for $(r, \theta, z) \in \mathcal{D}$ and $t > 0$. Equation (6) describes the nonlinear space-time evolution of the perturbation of the velocity field. Equation (7) is the solenoidal condition for the perturbation and Eqs. (8)–(10) describe the homogeneous boundary conditions for the radial coordinate and the periodic-boundary conditions for the azimuthal and axial coordinates, respectively, whereas Eq. (11) is the initial solenoidal condition for the perturbation field at $t=0$.

A. Spectral discretization

We discretize the perturbation \mathbf{u} by a solenoidal spectral approximation \mathbf{u}_S of order L in z , order N in θ , and order M in r ,

$$\mathbf{u}_S(r, \theta, z, t) = \sum_{l=-L}^L \sum_{n=-N}^N \sum_{m=0}^M a_{lmn}(t) \Phi_{lmn}(r, \theta, z), \quad (12)$$

where Φ_{lmn} are *trial* bases of solenoidal vector fields of the form

$$\Phi_{lmn}(r, \theta, z) = e^{i(lk_0 z + n\theta)} \mathbf{v}_{lmn}(r) \quad (13)$$

with $k_0=2\pi/\Lambda$, satisfying

$$\nabla \cdot \Phi_{lmn} = 0 \quad (14)$$

for $(l, n, m) \in [-L, L] \times [-N, N] \times [0, M]$. The trial bases (13) are therefore $(\Lambda, 2\pi)$ periodic in the axial and azimuthal directions, respectively. The radial functions \mathbf{v}_{lmn} appearing in Eq. (13) must satisfy homogeneous boundary conditions at the inner and outer radii of the cylinders,

$$\mathbf{v}_{lmn}(r_i, \theta, z) = \mathbf{v}_{lmn}(r_o, \theta, z) = \mathbf{0}. \quad (15)$$

The spectral scheme is accomplished when introducing expansion (12) in Eq. (6) and projecting over a suitable set of *test* solenoidal fields,

$$\Psi_{lmn} = e^{i(lk_0 z + n\theta)} \tilde{\mathbf{v}}_{lmn}. \quad (16)$$

Both sets \mathbf{v}_{lmn} and $\tilde{\mathbf{v}}_{lmn}$ can be found in the Appendix. The projection is carried out via the standard volume integral over the domain \mathcal{D} ,

$$(\Psi, \partial_t \mathbf{u}_S)_{\mathcal{D}} = (\Psi, \Delta \mathbf{u}_S - (\mathbf{v}_B + \mathbf{u}_S) \cdot \nabla (\mathbf{v}_B + \mathbf{u}_S))_{\mathcal{D}} \quad (17)$$

for all $\Psi = \Psi_{lmn}$ with $(l, n, m) \in [-L, L] \times [-N, N] \times [0, M]$, where

$$(\mathbf{a}, \mathbf{b})_{\mathcal{D}} = \int_{\mathcal{D}} \mathbf{a}^* \cdot \mathbf{b} d\mathcal{D}, \quad (18)$$

and where $*$ stands for complex conjugate. The pressure term is canceled in the projection [30], i.e., $(\Psi_{lmn}, \nabla q)_{\mathcal{D}} = 0$, leading to a dynamical system only involving the amplitudes $a_{lmn}(t)$ of the velocity approximation (12), i.e.,

$$\Lambda_{pqr}^{lmn} \frac{da_{pqr}}{dt} = \mathbb{B}_{pqr}^{lmn} a_{pqr} - \mathbb{N}_{lmn}(a, a), \quad (19)$$

where we have used the convention of summation with respect to repeated subscripts. In Eq. (19), the matrices Λ and

\mathbb{B} stand for the projection of the time differentiation and linear Laplacian-advection operators, whereas \mathbb{N} is the projected nonlinear advective term. System (19) is integrated in time by means of an implicit fourth-order backward difference method for the linear part with fourth-order polynomial extrapolation for the nonlinear terms. Overall, the solenoidal scheme used here is mainly based on previous spectral schemes recently formulated and extensively tested for cylindrical and annular geometries [1,13,31,32]. The computations presented in this paper have been carried out for $\eta = 0.883$, $R_o = -1200$, and $R_i \in [400, 600]$. All results shown here are spectrally resolved. The spectral resolution used was always within the range $(L, N, M) \in [14, 24] \times [14, 24] \times [16, 32]$. An increase in the spatial resolution did not provide noticeable improvement.

B. Computation of rotating waves: Newton-Krylov methods and azimuthal subspaces

For azimuthally rotating waves, we reformulate the problem in a suitable *corotating frame* such that the sought solution is steady in that coordinate system. Henceforth, we assume that the perturbation field satisfies

$$\mathbf{u}(r, \theta, z, t) = \mathbf{u}(r, \theta - c_\theta t, z, 0), \quad \forall t > 0, \quad (20)$$

with c_θ the *a priori* unknown azimuthal phase speed of the wave. Relation (20) implicitly imposes the time dependence structure of the coefficients $a_{lm}(t)$ appearing in our spectral expansion (12) to be

$$a_{lm}(t) = \hat{a}_{lm} e^{-inc_\theta t}. \quad (21)$$

Formal substitution of Eq. (12) restricted to the coefficient form (21) in Eq. (6) leads to a time-independent nonlinear algebraic system,

$$\mathbb{F}_{nl}(\hat{a}, c_\theta) \equiv \{inc_\theta \mathbb{A} + \mathbb{B}\} \hat{a}_{lm} + \mathbb{N}(\hat{a}). \quad (22)$$

The solenoidal spectral formulation allows us to decouple the system for each (n, l) azimuthal-axial pair. This nonlinear system of equations is solved with a *Newton-Krylov* method using GMRES (generalized minimum residual method) [33] algorithm at every iteration. This algorithm is embedded within an *arclength* continuation scheme that allows us to follow the branch of the corresponding solution parametrized in R_i [34]. The method described here has been successfully applied in the computation of traveling wave solutions in pipe flow [13,32].

Newton methods require suitable initial seeds for \hat{a} and c_θ in order to converge to the solution. This can be accomplished by initially approaching to the rotating wave with time integration (provided that this solution is stable) and then estimating its speed. Another option consists in using the linear stability analysis of the CCF and computing the unstable eigenvectors and eigenvalues nearby the bifurcation point. In general, bifurcating spirals in counter-rotating TCF are unstable and they cannot be approached using the Navier-Stokes time-marching scheme. These spirals are typically unstable with respect to other helicoidal perturbations and therefore it is necessary to restrict the time integration under some specific helicoidal subspace. In some cases, the

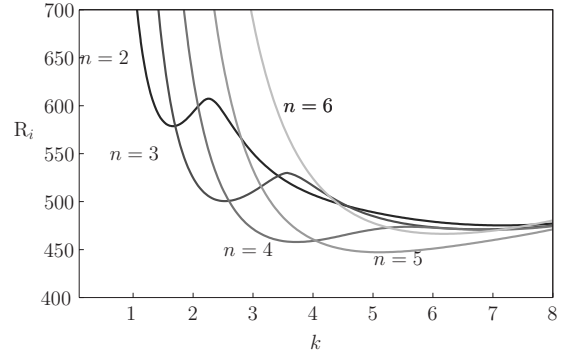


FIG. 1. Neutral stability curves corresponding to the most critical azimuthal modes ($2 \leq n \leq 6$) for $R_o = -1200$ and $\eta = 0.883$.

time integrations will be carried out within axial-azimuthal subspaces with a fixed helicoidal slope in order to avoid interactions with other spiral solutions. In those cases, the spectral approximation (12) has the particular form

$$\mathbf{u}(r, \theta, z, t) = \sum_{\ell=-L}^L \sum_{m=0}^M a_{\ell m}(t) e^{i\ell(k_0 z + n_0 \theta)} \mathbf{v}_{\ell \bar{n} m}(r), \quad (23)$$

where $\bar{n} = \ell n_0$ and with n_0 fixing the spiral shape, i.e., the computed spirals have a fixed helicoidal orientation with angle $\tan \phi = -n_0 / k_0$.

III. RESULTS

The linear stability of the CCF is governed by the real part $\sigma(n, k)$ of the rightmost eigenvalue of the spectrum of the linearized Navier-Stokes operator $\mathbb{L} = \mathbb{A}^{-1} \mathbb{B}$ of Eq. (19) for any $(n, k) = (n, lk_0)$ azimuthal-axial pair. The neutral stability curves result from imposing $\sigma(k, R_i) = 0$ for fixed n , R_o , and η . These curves are shown in Fig. 1 for $R_o = -1200$, $\eta = 0.883$, and $n \in [0, 6]$. The critical azimuthal mode is $n_c = \pm 5$ for $k_c = 5.125$ and $R_i^c = 447.35$. Therefore, for $R_i > R_i^c$, the first instability leads to a *spiral flow* (SF) with two possible helicoidal orientation angles $\tan \phi = \pm k_c / n_c$. The SF regime evolves to more complex flows as R_i is further increased due to the presence of the nearby unstable azimuthal modes $n = \pm 4, \pm 6$.

In the first part of our exploration, the computations were carried out for the two first destabilized axial wave numbers $k_0 = 5.125$ and $k_0 = 3.76$, corresponding to the critical values at instability of the azimuthal modes $n = 5$ and $n = 4$, respectively. The aspect ratio of the computational box is fixed with value $\Lambda = 2\pi / k_c$ in each case. For $R_i > R_{ic}$, forward time integration will generally lead to a destabilization of the basic flow that does not converge to a specific spiral mode. Instead, spirals of different azimuthal symmetries compete above the critical threshold and the dynamics of the problem becomes very complex, leading to interpenetrating spirals, wavy spirals, or even chaotic flows.

A. Short-wavelength rotating waves

For $n_0 \in [1, 6]$, we start with a random perturbation destabilizing the flow far beyond the inner rotation critical value

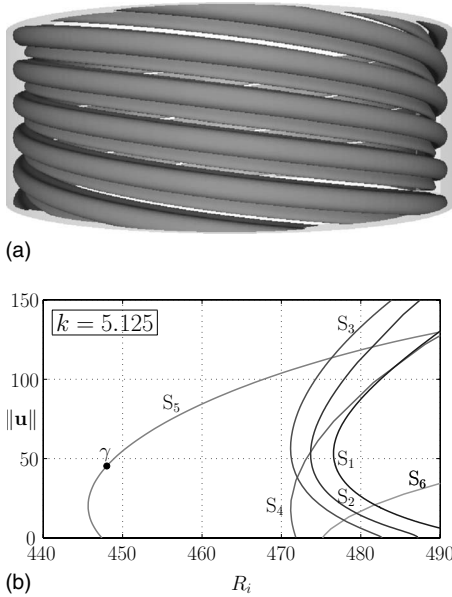


FIG. 2. (a) Angular-momentum $L = rv_\theta$ isosurfaces of the S_5 spiral mode for $R_i = 448$ [point γ in (b)]. (b) Continuation curves of the S_{n_0} spiral solutions as a function of R_i for $1 \leq n_0 \leq 6$; $k_0 = 5.125$.

($R_i = 500$); symmetry reduced time integration results in a spiral mode with the prescribed symmetry, converging to the stable upper branch of the bifurcated solution. The Newton-Krylov method is applied afterward using the almost converged spiral as initial seed, continuing the spiral mode as a function of the inner Reynolds number and tracking it back to its connection with the basic flow. Figure 2(a) shows the angular-momentum distribution corresponding to the S_5 mode for $R_i = 448$. This spiral solution is represented by the point γ in the continuation curve corresponding to the $n_s = 5$ family shown in Fig. 2(b).

Arclength continuation of the S_5 mode confirms that this spiral flow is subcritical. The S_5 mode is born in a saddle-node bifurcation at $R_i = 445.65$ slightly below the critical value provided by the linear stability analysis. The continuation algorithm allowed us to compute the lower unstable saddle branch that reconnects with the base flow at $R_i = 447.35$. The other spiral flows from S_2 to S_6 were similarly computed; all of them but S_6 were found to be subcritical. The saddle nodes of the subcritical spirals were found to be substantially far away from their connections with the CCF. In particular, subcriticality of $S_{1,2,3}$ spirals is much more pronounced than the rest, as shown in Fig. 2(b).

The second dominant mode in the linear stability analysis is $n = \pm 4$ with associated axial wave number $k_0 = 3.76$ and $R_i^c = 458$. In this case, we found richer bifurcation phenomena, as shown in Fig. 3. For $k_0 = 3.76$, the first instability leads to an S_4 supercritical spiral. The only S_1 spiral found is actually an S_2 spiral with doubled axial periodicity (that we termed as $S_2^{2k_0}$). The $S_2^{2k_0}$ solution was found to be highly subcritical with a connection with the CCF at $R_i = 475.7$ and a saddle-node point near $R_i = 460.1$. Surprisingly, no pure S_2 spiral mode was found to bifurcate locally from the basic flow. Instead, the only S_2 mode identified came out from a pitchfork bifurcation of another $n = 4$ spiral, S_4^a . The S_4^a

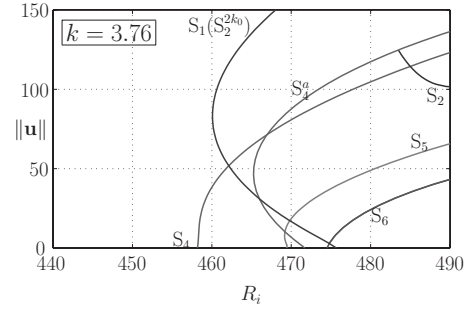


FIG. 3. Norm of the S_{n_0} spiral solutions as a function of R_i for $k_0 = 3.76$ and $1 \leq n_0 \leq 6$.

branch is born at a secondary subcritical Hopf bifurcation of CCF at $R_i = 471.7$, exhibits a saddle-node turning point at $R_i = 465.25$, and undergoes a pitchfork bifurcation to a pure S_2 mode at $R_i = 483.5$. As in the case for $n_s = 2$ previously described, time integrations in the n_3 subspace never converged to pure S_3 spiral modes. These modes only appeared from pitchfork bifurcations of a S_6 spiral for $R_i > 500$. Finally, S_5 has similar features as S_5 for $k_0 = 5.125$.

B. Continuation to lower axial wave numbers

The computed spiral regimes originate from the CCF at Hopf bifurcations; some of them are of subcritical nature. Their instability is clearly related to centrifugal mechanisms and their axial wavelength is consistent with the characteristic width of the inner centrifugally unstable region $r \in [r_i, r_{\text{nod}}]$, with r_{nod} being the nodal radius satisfying $v_B(r_{\text{nod}}) = 0$. Spiral flows with higher azimuthal and axial wave numbers tend to be less subcritical, whereas spirals with lower azimuthal and axial wave numbers, although not dominant at transition, clearly show more pronounced subcriticality. This motivates further exploration for lower values of k_0 in order to find the large-scale axial dynamics typical of spiral turbulence. However, straightforward continuation of the spirals shown above for lower values of k_0 was unsuccessful. The origin of the problem lies within the discontinuous nature of the spectra of rightmost eigenvalues corresponding to the CCF as a function of k . A closer look to the neutral stability curves shown in Fig. 1 for lower azimuthal-axial wave numbers reveals the presence of secondary radial eigenmodes which become dominant in the linearly stable shear region $r \in [r_{\text{nod}}, r_o]$ for considerably lower values of k . This *double-minima* phenomenon is well known in the literature of axially driven annular flows [35,36], although it has been overlooked for the case of purely azimuthal shear flow. As an example, the azimuthal mode $n = 3$ has a critical axial wave number $k \sim 6.8$ for $R_i \sim 471.1$ and a secondary local minimum for $k \sim 2.5$ for $R_i \sim 500.45$. Figure 4 shows the real part of the rightmost eigenvalues of the linearized Navier-Stokes operator for $R_i = 470$ and $R_i = 500$ as a function of k . Both eigenvalues correspond to independent instability mechanisms, as their eigenmode structure at bifurcation shows in Fig. 5. As a result, the continuation curves of the previously found spiral solutions exhibit turning points before k reaches lower values.

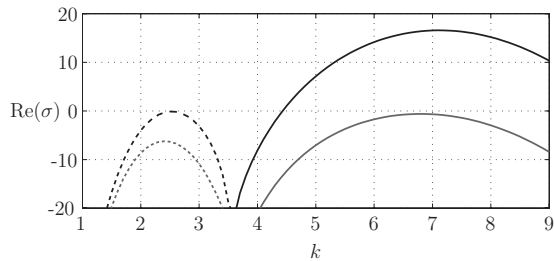


FIG. 4. Shear (dashed curve) and centrifugal (continuous curve) leading eigenvalue real parts of azimuthal mode $n=3$ for $R_i=470$ (gray) and $R_i=500$ (black).

As shown in Fig. 4, the CCF also becomes unstable with respect to perturbations of lower k for slightly higher inner Reynolds number R_i . These are primary instabilities also issued from local Hopf bifurcations of the CCF, thus leading to another family of spirals. These bifurcating spirals can barely be observed for a very short lapse of time when starting from initial conditions proportional to the eigenvector associated to the second bifurcating eigenvalue. However, after some short transient period, the spirals associated with the centrifugal mechanism (associated with the rightmost positive eigenvalue) take over the dynamics, being impossible to use this transient time integration as a successful initial guess for the Newton-Krylov method.

The computation of these spiral shear modes required two different techniques. The first one consisted of artificially cutting off the range of active axial modes (typically, $k_0L \lesssim 3.0$) in order to avoid linear instability of the centrifugal branch during the time evolution. By drastically reducing the number of axial modes in the Navier-Stokes solver, it was possible to reproduce an unresolved rotating wave. This numerical artifact was then used as initial seed in the Newton-Krylov method, later recovering spectral accuracy by increasing L the algorithm and recovering spectral accuracy again. The second technique was based on a quasistatic *homotopy* transformation in η , combined with an axial forcing. By including axial advection and reducing η it was possible to find other spirals of larger wavelength. A very careful variation of these two combined effects sometimes succeeded in recovering low axial wave-number rotating waves

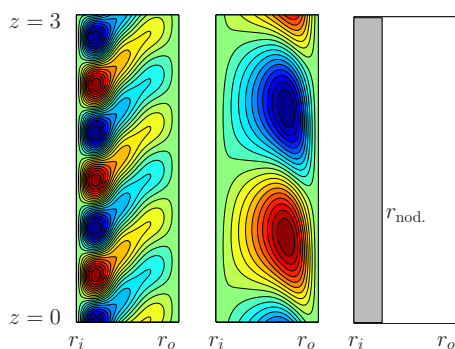


FIG. 5. (Color online) Eigenstream functions corresponding to the bifurcating centrifugal (left) and shear (center) radial modes for $R_i=470$ and $R_i=500$, respectively. On the right, shaded region shows the centrifugally unstable radial domain bounded by $r=r_{\text{nod}}$.

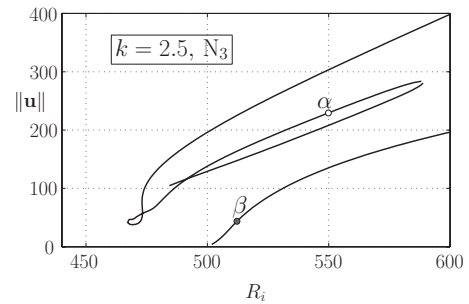


FIG. 6. Continuation curves of the ribbon solution (top, α) and spiral waves S_3 (bottom, β) as a function of R_i for $k_0=2.5$.

for our original problem. However, the described procedures have only been successful for $n_0=2$ and $n_0=3$ cases.

Two families of other solutions have been found. One of them is spirals that bifurcate supercritically from the CCF. The other family consists of *ribbons*, apparently disconnected from the CCF. Figure 6 shows both families for $k_0=2.5$, where the lower branch corresponds to a supercritical spiral family whose inner structure is detailed in Figs. 8(c) and 9(c). The upper branch shown in Fig. 6 corresponds to a ribbons' family represented in Figs. 8(b) and 9(b). This last curve has a more intricate structure with two turning points. According to our computations, our continuation scheme could not find a connection between this branch and the CCF. With the aforementioned cutoff and homotopy techniques we managed to compute other families of spirals with a lower axial wave-number limit of $k_0=1.7$. Figure 7 shows this branch whose longer axial structure is clearly visualized in Figs. 8(d) and 9(d). Unfortunately, none of these longer spirals have been found to be subcritical. These families of waves are characterized by having active dynamics in the outer radial wall as can be seen in the vorticity distributions shown in Fig. 8.

IV. CONCLUSIONS

We have explored the skeleton of equilibrium solutions for Taylor-Couette flows in small-gap counter-rotating situations. This has been done for a fixed value of the outer Reynolds number where experimentalists have detected intermittency phenomena. Our results confirm that the Hopf bifurcations that lead to spiral secondary regimes are of subcritical nature in many cases. These spirals are in general

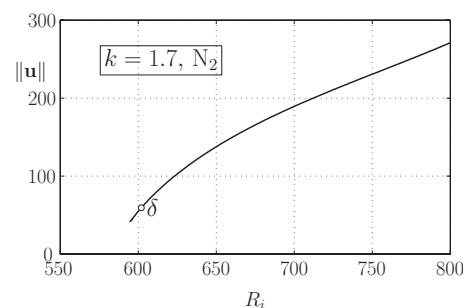


FIG. 7. Continuation curve of the S_2 solution as a function of R_i for $k_0=1.7$.

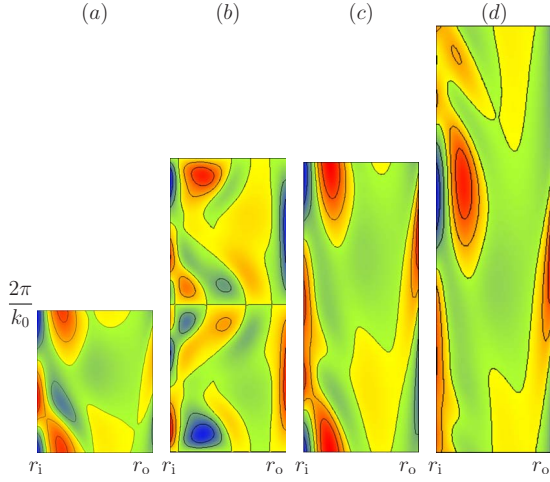


FIG. 8. (Color online) Contours of azimuthal vorticity $(\nabla \times \mathbf{u})_\theta$ for three different families of rotating waves in $\theta = \text{const.}$ section within $(r, z) \in [r_i, r_o] \times [0, 2\pi/k_0]$. (a) S_5 spiral mode corresponding to point γ in Fig. 2 at $R_i=448$ and $k=5.125$. (b) Ribbon corresponding to point α in Fig. 6 at $R_i=500$ and $k_0=2.5$. (c) S_3 spiral corresponding to point β in Fig. 6 at $R_i=512.2$ and $k_0=2.5$. (d) S_2 spiral corresponding to point δ in Fig. 7 at $R_i=601.9$ and $k_0=1.7$.

unstable with respect to perturbations of different helicities, although they may be stable in their own helicoidal subspace. The spirals arising from the first bifurcation of the CCF have short axial wavelengths and their dynamics is confined within the centrifugally unstable radial layer. Other families of rotating spirals born in bifurcations of secondary eigenvalues with longer axial wavelength have been identified by means of an initial severe truncation of the axial wave-number range, thereafter recovering spectral accuracy with the Newton-Krylov method. Rotating ribbons have also been found by homotopy transformations in the radius ratio combined with axial advection forcing. Quasistatistical recovery of the original values sometimes succeeded in finding this exotic type of solution. Continuation of the ribbon family did not reconnect with the basic flow. Overall, the subcritical nature of the bifurcating spirals might shed some light on the intermittency phenomena that experimentalists have found in nearby regions of the parameter space and for the same radius ratio. This work addresses the exploration of equilibria in a problem that can be an excellent experimental and theoretical framework to study subcritical transition to turbulence in shear flows. However, further exploration should be carried out for higher outer rotations in order to confirm whether the subcriticality of these invariant solutions gets more pronounced and can therefore account for hysteretic phenomena observed in experiments. Other laminar secondary regimes such as interpenetrating spirals should be explored as well. These and other tasks will be carried out in future investigations.

ACKNOWLEDGMENTS

This work was supported by the Spanish Government under Grants No. FIS2007-61585 and No. AP-2004-2235 and by the Catalanian Government under Grant No. SGR-00024.

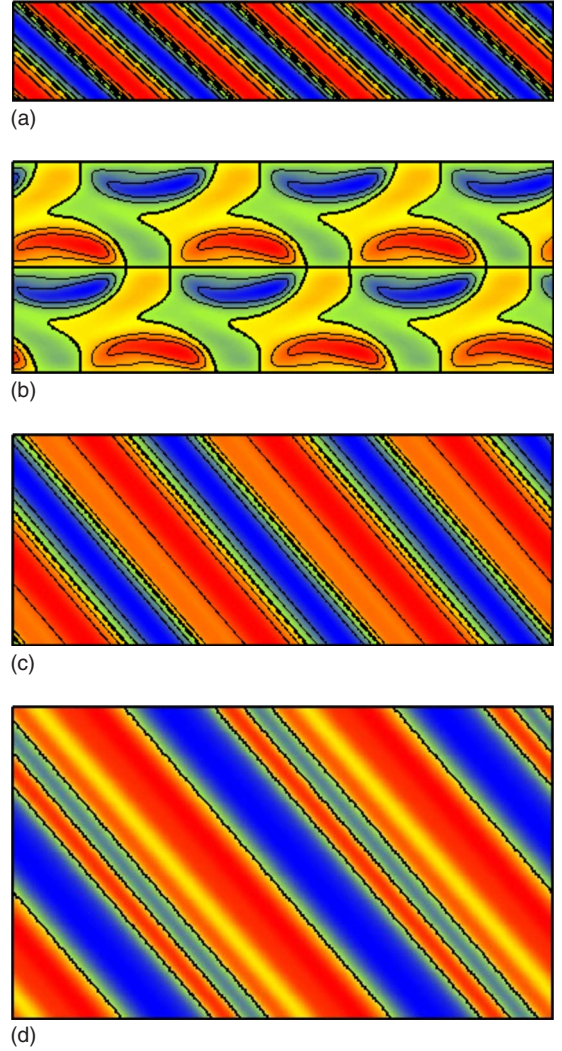


FIG. 9. (Color online) (a)–(d) Same as in Fig. 8, showing contours of radial vorticity $(\nabla \times \mathbf{u})_r$ in $r = \text{const.}$ section within $(\theta, z) \in [0, 2\pi] \times [0, 2\pi/k_0]$.

APPENDIX: SOLENOIDAL SPECTRAL BASES

In what follows, we define

$$\delta = \frac{1 + \eta}{1 - \eta}, \quad x(r) = 2r - \delta \tag{A1}$$

that maps the radial domain $r \in [r_i, r_o]$ to the interval $x \in [-1, 1]$ and

$$h_m(r) = (1 - x^2)T_m(x), \quad g_m(r) = (1 - x^2)^2T_m(x), \tag{A2}$$

where $T_m(r)$ is the Chebyshev polynomial of degree m and $w(x) = 1/\sqrt{1-x^2}$ is the weight function within the interval $(-1, 1)$. The functions in Eq. (A2) satisfy

$$h_m(r_i) = h_m(r_o) = 0, \tag{A3}$$

$$g_m(r_i) = g_m(r_o) = Dg_m(r_i) = Dg_m(r_o) = 0, \tag{A4}$$

where D stands for the radial differentiation operator d/dr .

The trial basis for axisymmetric fields ($n=0$) is given by

$$\mathbf{v}_m^{(1)}(r) = \begin{pmatrix} 0 \\ h_m \\ 0 \end{pmatrix}, \quad \mathbf{v}_m^{(2)}(r) = \begin{pmatrix} -ilk_0 r g_m \\ 0 \\ D(r g_m) + g_m \end{pmatrix}, \quad (\text{A5})$$

except that the third component of $\mathbf{v}_m^{(2)}$ is replaced with h_m when $l=0$, whereas for the nonaxisymmetric case the basis is

$$\mathbf{v}_m^{(1)}(r) = \begin{pmatrix} -i n g_m \\ D(r g_m) \\ 0 \end{pmatrix}, \quad \mathbf{v}_m^{(2)}(r) = \begin{pmatrix} 0 \\ -ilk_0 r h_m \\ i n h_m \end{pmatrix}, \quad (\text{A6})$$

except that the third component of $\mathbf{v}_m^{(2)}$ is replaced by h_m when $l=0$. For the projection space, the basis corresponding to axisymmetric fields is

$$\tilde{\mathbf{v}}_m^{(1)}(r) = w(x) \begin{pmatrix} 0 \\ r h_m \\ 0 \end{pmatrix}, \quad (\text{A7})$$

$$\tilde{\mathbf{v}}_m^{(2)}(r) = r^{-2} w(x) \begin{pmatrix} ilk_0 g_m \\ 0 \\ D_+ g_m + 2r^{-1}(1-x^2+rx)h_m \end{pmatrix}, \quad (\text{A8})$$

where $D_+ = D + 1/r$ and the third component of $\tilde{\mathbf{v}}_m^{(2)}$ is replaced by $r h_m$ if $l=0$. The basis for the nonaxisymmetric case is

$$\tilde{\mathbf{v}}_m^{(1)}(r) = w(x) \begin{pmatrix} i n r g_m \\ r D_+(r g_m) + 2x r^2 h_m \\ 0 \end{pmatrix}, \quad (\text{A9})$$

$$\tilde{\mathbf{v}}_m^{(2)}(r) = w(x) \begin{pmatrix} 0 \\ ilk_0 r^2 h_m \\ -i n r h_m \end{pmatrix}. \quad (\text{A10})$$

-
- [1] A. Meseguer and L. N. Trefethen, *J. Comput. Phys.* **186**, 178 (2003).
- [2] V. A. Romanov, *Funct. Anal. Appl.* **7**, 137 (1973).
- [3] S. A. Orszag, *J. Fluid Mech.* **50**, 689 (1971).
- [4] M. Nishioka, S. Iida, and Y. Ichikawa, *J. Fluid Mech.* **72**, 731 (1975).
- [5] S. A. Orszag and L. C. Kells, *J. Fluid Mech.* **96**, 159 (1980).
- [6] S. A. Orszag and A. T. Patera, *J. Fluid Mech.* **128**, 347 (1983).
- [7] A. T. Patera and S. A. Orszag, *J. Fluid Mech.* **112**, 467 (1981).
- [8] M. Nagata, *J. Fluid Mech.* **217**, 519 (1990).
- [9] A. Cherhabili and U. Ehrenstein, *J. Fluid Mech.* **342**, 159 (1997).
- [10] H. Faisst and B. Eckhardt, *Phys. Rev. Lett.* **91**, 224502 (2003).
- [11] H. Wedin and R. R. Kerswell, *J. Fluid Mech.* **508**, 333 (2004).
- [12] J. F. Gibson, J. Halcrow, and P. Cvitanovic, *J. Fluid Mech.* **611**, 107 (2008).
- [13] F. Mellibovsky and A. Meseguer, *Philos. Trans. R. Soc. London, Ser. A* **367**, 545 (2009).
- [14] F. Waleffe, *Phys. Fluids* **15**, 1517 (2003).
- [15] F. Waleffe, *Phys. Fluids* **9**, 883 (1997).
- [16] J. M. Hamilton, J. Kim, and F. Waleffe, *J. Fluid Mech.* **287**, 317 (1995).
- [17] J. Jimenez and P. Moin, *J. Fluid Mech.* **225**, 213 (1991).
- [18] B. Hof, C. W. H. van Doorne, J. Westerweel, F. T. M. Nieuwstadt, H. Faisst, B. Eckhardt, H. Wedin, R. R. Kerswell, and F. Waleffe, *Science* **305**, 1594 (2004).
- [19] B. Hof, J. Westerweel, T. M. Schneider, and B. Eckhardt, *Nature (London)* **443**, 59 (2006).
- [20] D. Barkley and L. S. Tuckerman, *Phys. Rev. Lett.* **94**, 014502 (2005).
- [21] G. I. Taylor, *Philos. Trans. R. Soc. London, Ser. A* **223**, 289 (1923).
- [22] C. D. Andereck, S. S. Liu, and H. L. Swinney, *J. Fluid Mech.* **164**, 155 (1986).
- [23] P. Chossat and G. Iooss, *The Couette-Taylor Problem*, in *Applied Mathematical Sciences Vol. 102* (Springer-Verlag, New York, 1994).
- [24] R. Tagg, *Nonlinear Sci. Today* **4**(3), 1 (1994).
- [25] D. Coles, *J. Fluid Mech.* **21**, 385 (1965).
- [26] C. W. Van Atta, *J. Fluid Mech.* **25**, 495 (1966).
- [27] A. Meseguer, *Phys. Fluids* **14**, 1655 (2002).
- [28] A. Prigent, G. Gregoire, H. Chate, O. Dauchot, and W. van Saarloos, *Phys. Rev. Lett.* **89**, 014501 (2002).
- [29] H. Faisst and B. Eckhardt, *Phys. Rev. E* **61**, 7227 (2000).
- [30] C. Canuto, M. Y. Hussaini, A. Quarteroni, and T. A. Zang, *Spectral Methods in Fluid Dynamics* (Springer-Verlag, New York, 1988).
- [31] A. Meseguer, *Phys. Fluids* **15**, 1203 (2003).
- [32] A. Meseguer, M. Avila, F. Mellibovsky, and F. Marques, *Eur. Phys. J. Spec. Top.* **146**, 249 (2007).
- [33] L. N. Trefethen and D. Bau, *Numerical Linear Algebra* (SIAM, Philadelphia, 1997).
- [34] Y. A. Kuznetsov, *Elements of Applied Bifurcation Theory*, in *Applied Mathematical Sciences Vol. 112* (Springer-Verlag, New York, 2004).
- [35] B. S. Ng and E. R. Turner, *Proc. R. Soc. London, Ser. A* **382**, 83 (1982).
- [36] A. Meseguer and F. Marques, *J. Fluid Mech.* **402**, 33 (2000).